Chapter 2
Structural Evolution of the Thermally Reduced Graphene Nanosheets During Annealing

2.1 Introduction

Supercapacitor, also called electrochemical capacitor or ultracapacitor, is considered to be one of the newest innovations in the field of electrical energy storage. Compared to the battery devices, it is not limited by the electrochemical charge transfer kinetics of batteries, and thus owns unique advantages in high power density (10 kW kg^{-1}), short charge/discharge duration (in seconds), and long cycle life (over a million cycles) [1, 2]. These features have made supercapacitors very popular in various applications, such as hybrid electric vehicles, electric tools, and industrial power management [3].

Carbon materials are regarded as the first candidate electrode materials for supercapacitors [4, 5]. On one hand, charge storage on carbon electrodes is predominantly capacitive based on the electric double-layer capacitor (EDLC) through the electrostatic attraction of electrolyte ions onto the surface of carbon materials. On the other hand, contributions from surface functional groups can also be charged and discharged depending on Faradic redox reactions to yield pseudocapacitance (PC) [6].

Among various carbon allotropes, graphene shows competitive advantages in electrochemical energy storage applications, such as supercapacitors and Li ion batteries owing to its unique two-dimensional structure, high electronic conductivity, huge surface area, and good chemical stability [7–11]. Since the thermally reduced graphene (TRG) can be reliably obtained by thermal exfoliation of graphite oxide (GO), the chemical method became the strategic starting point for scale-up production of graphene [12–17]. As inherited from the precursor GO, TRG is instinctively decorated by various active sites (e.g., heteroatoms and lattice defects), which is essential with respect to providing a fertile ground for surface chemistry of carbon. The functionality, microtexture, polarization, acid/basic, as well as electronic properties of graphene can be easily tailored by adjusting the degree of thermal annealing [18]. The promising properties together

C.-M. Chen, *Surface Chemistry and Macroscopic Assembly of Graphene for Application in Energy Storage*, Springer Theses,
DOI 10.1007/978-3-662-48676-4_2

with the ease of processability and functionalization make graphene an ideal candidate for developing high performance supercapacitors [19–29]. It has reported that the ultimate performance of graphene-based supercapacitors will be bound up with the physical and chemical characteristics of graphene electrodes [22–24, 28]. Thus, a deep understanding of the structural evolution of graphene during annealing process is desirable for matching chemical surface properties with supercapacitor applications, which provides further new insights into the design of advanced energy storage devices in industry.

In this chapter, the TRG was produced by vacuum promoted thermal expansion of GO at relatively low temperatures, and the surface chemistry of which was further tuned by progressive annealing at various temperatures. Additionally, the structural evolution (microtexture, pore structure, type, and density of residue functionalities) of TRGs was investigated, while the electrochemical performance of which as supercapacitor electrodes was also evaluated.

2.2 Experimental

2.2.1 Preparation of TRG

The TRG was prepared by rapid heating up of GO under high vacuum [14]. GO was obtained by a modified Hummers' method [30]. The as-obtained GO was grounded into fine powder (~100 mesh), and air dried at 100 °C for 3.0 h. Then it was put into a quartz tube that was sealed at one end and stopped at the other end, through which the reactor was connected to a vacuum pump. The tube was heated at a rate of 30 °C min^{-1} in high vacuum (<2 Pa). At about 200 °C, an abrupt expansion was observed. The further annealing process of the above expanded GO was carried out at 250, 600, 800, and 1000 °C for 20 min, respectively. Finally, a series of graphene samples with different surface functionalities were obtained, which are named GT, where T represents the further annealing temperature. During the whole exfoliating and annealing process, a high vacuum in the quartz tube with a pressure of less than 5.0 Pa was maintained, as the vacuum pump was kept onto suck the desorbed gas out of the tube.

2.2.2 Sample Characterization

Scanning electron microscope (SEM) investigations were carried out with a JEOL JSM 7401F operated at 2.0 kV and a JEOL JEM 2010 transmission electron microscope (TEM) operated at 200.0 kV. The samples were ultrasonically dispersed in ethanol, and a drop of the solution was deposited on a Lacey carbon film grid for TEM characterization; X-ray diffraction (XRD) patterns were obtained at room

temperature using specular reflection mode (Cu Kα radiation, λ = 0.15406 nm, D8 Advance, BRUKER/AXS, Germany); Laser Raman spectroscopy was performed on powder samples by using an ISA LabRam instrument equipped with an Olympus BX40 microscope. The excitation wavelength was 632.8 nm and a spectral resolution of 0.9 cm^{-1} was used; N_2 adsorption isotherm was measured using a Micromeritics 2375 at 77 K. The specific surface area was calculated by the Brunauer-Emmett-Teller (BET) method, the surface area of micropores (S_{micro}) was calculated by the t-plot approach (plot range from 3.5 to 5 nm), and the pore size distribution was deduced from the desorption isotherm by the Barret-Joyner-Halenda (BJH) method; Fourier transform infrared spectroscopy (FTIR) spectrums were carried out on a Thermo Nicolet IR200 spectrometer and the sample was pre-pressed with KBr into pellets before test; X-ray photoelectron spectroscopy (XPS) was obtained on the Thermo VG ESCALAB250 surface analysis system with parameters: Al Kα = 1486.6 eV, Power = 150 W (HV = 15 kV and I = 10 mA), spot size = 500 μm, pass energy 50.0 eV and energy step size 0.1 eV; the as-obtained graphene samples were further performed using thermal gravimetric analysis (TGA) system (STA 409 PC Luxx, Netzsch, Germany) equipped with a sweep gas mass spectroscopy appliance (ALZERS OmniStar 20, Switzerland).

2.2.3 Electrochemical Measurements

Electrochemical measurements of TRGs were performed using a three-electrode system in 6.0 M KOH aqueous solution, whereas Ni foam coated with electrode materials served as the working electrode, a platinum foil electrode as the counter electrode, and a reversible hydrogen electrode (RHE) as the reference electrode. The working electrodes were prepared as following: a mixture of the active material, carbon black, and poly (tetrafluoroethylene) (PTFE) with a weight ratio of 80:5:15 was ground together to form homogeneous slurry. The slurry was squeezed into a film and then punched into pellets (area ~0.8 cm^2). The punched pellets with a piece of nickel foam on each side were pressed under 2.5 MPa and dried overnight at 110 °C. Each working electrode contained ~3.5 mg electroactive materials. The electrodes were saturated with the electrolyte by vacuum enhanced impregnation for 2.0 h prior to the electrochemical evaluation. Cyclic voltammetry (CV) curves, galvanostatic charging/discharging (GC) curves and electrochemical impedance spectroscopy (EIS) profiles (frequency from 200 kHz to 10 mHz) were measured with a BioLogic electrochemistry workstation. The specific capacitances (C_F, F g^{-1}) were calculated from CV curves by equation: $C_F = S_{int}/(2\ V_s\ m)$, where S_{int} in mA V is the integrated area of CV curves, V_s in mV s^{-1} is the sweep rate, and m in g is the weight of active materials in the electrode. The Nyquist plots were fitted by the EC-Lab software with the equivalent circuit as $R_c + C_c/(R_i + W) + C_d$, the Randomize plus Levenberg–Marquardt method was employed for the fitting. The Ragone plot was calculated from GC results, the energy density (E, Wh kg^{-1}) was calculated by

equation: $E = 1/2 * (C_F/4) * U^2$, where U is the potential window employed for GC (1.0 V in this work). While power density (P, W kg^{-1}) was calculated by: $P = E/t$, whereas t in s is the current drain time of discharging [1, 6].

2.3 Results and Discussion

2.3.1 Structural Evolution

The TRG was prepared by vacuum promoted thermal exfoliation of GO. Figure 2.1a shows a huge volume expansion obtained through the transformation from GO to TRG. In a typical procedure, ~0.6 g of TRG (G250) was produced by exfoliating 1.0 g of GO dry powder. Figure 2.1b, c show the SEM images of GO and G250. It can be seen that GO exhibits compact bulk morphology, while G250 owns a 3D honeycomb-like nanostructure. Numerous exterior macropores can be clearly identified among the lateral edges of graphene sheets. After high temperature annealing as shown in Fig. 2.1d, G1000 still maintained a honeycomb-like structure. However, a basal plane with a quite irregular edge is identified in G250 (Fig. 2.1e inset), while a more graphitic texture with a trimming edge can be found in G1000 (Fig. 2.1f inset), as indicated by the TEM.

N_2 adsorption isotherm, XRD and Raman spectroscopy were employed to investigate the morphological and structural evolution from graphite to TRG. As shown in Fig. 2.2a, all the isotherms give rise to a similar type III isotherm with H3 hysteresis loop in IUPAC classification, implying a unique adsorption behavior in the slit-shaped macropores raised from aggregates of plate-like particles. The specific BET surface area (S_{BET}), t-plot micropore surface area ($\Phi < 2$ nm) (S_{micro}), and total pore volume (V_P) of RGs are shown in Table 2.1. It is noteworthy that the S_{BET} is dramatically increased from 46.4 $m^2\ g^{-1}$ of precursor GO to 308.8 $m^2\ g^{-1}$ of G250, and the value keeps steady around 300 $m^2\ g^{-1}$ for G600 and G800, however raises to 434.1 $m^2\ g^{-1}$ for G1000. Besides, all the TRGs afford large pore volumes (V_P) of ~3 mL g^{-1}, which are higher than most of the ordered porous carbon materials (usually less than 1 mL g^{-1}) [31–34]. The BJH adsorption pore size distribution of G250 and G1000 (Fig. 2.2b) and t-plot micropore data (Table 2.1) indicate that the surface area and pore volume is mainly dependent on the pores with larger diameters ($\Phi > 2$ nm).

The XRD patterns of all the samples are given in Fig. 2.2c. The interlayer space (d_{002}) is increased from 0.334 nm of graphite to 0.698 nm of GO due to the efficient chemical intercalation by functional groups and water, which indicates an efficient transformation from GO to graphene. Furthermore, all TRG samples exhibit very weak diffraction peaks, owing to the dissociation of long-range ordered stacking of GO by random interlayer expansion and exfoliation [35].

The nature of disorder in GO and TRG is further studied by Raman spectroscopy (Fig. 2.2d). The in-plane vibration of a sp^2-hybridized carbon in the graphite crystallites (G band) as well as the disorder band aroused from amorphous carbon and

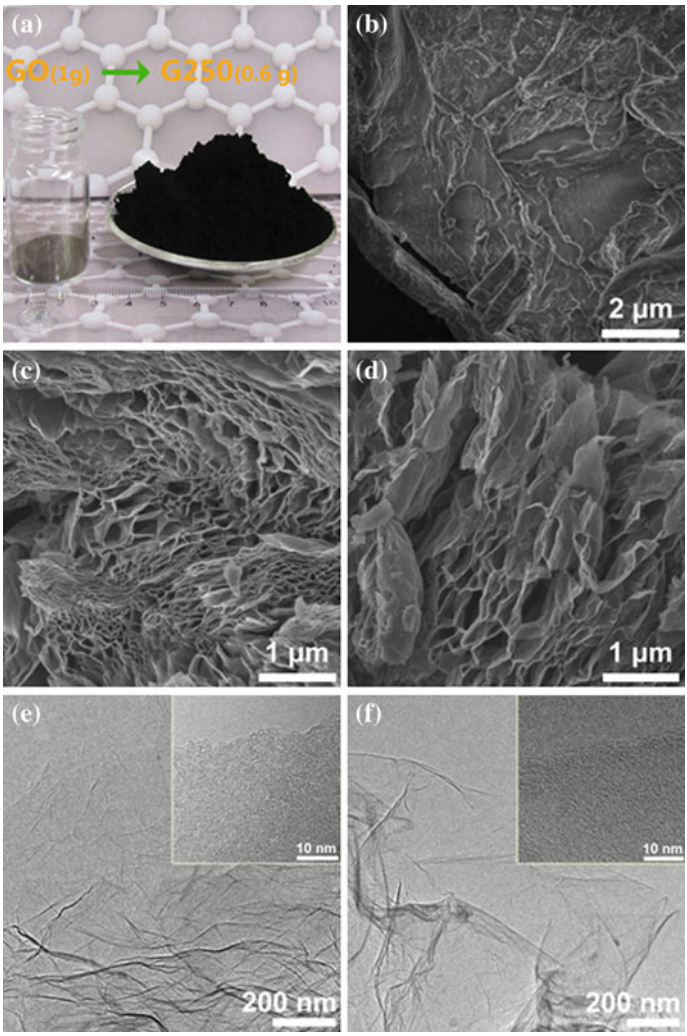

Fig. 2.1 **a** Digital images of the GO precursor (1.0 g) and resulted G250 (~600 mg); SEM images of **b** GO, **c** G250, and **d** G1000; TEM images of **e** G250 and **f** G1000. *Inserted figures* are the high resolution TEM images of **e** G250 and **f** G1000. Reprinted from Ref. [55], Copyright 2012, with permission from Elsevier

edges (D band) are identified, respectively. The peak positions and I_D/I_G ratios as calculated from Raman spectra (Fig. 2.2d) are provided in Table 2.1. Along the graphite-GO-TRG path, both the D and G band undergo significant changes upon amorphization of graphite, as amorphous carbon contains a certain fraction of sp^3 carbons. First, from graphite to GO, the G band widens significantly with a blue

Table 2.1 Summary of pore structure and elemental composition of TRG

Sample	D band[a] (cm^{-1})	G band[a] (cm^{-1})	I_D/I_G[a]	S_{BET}[b] ($m^2\ g^{-1}$)	S_{micro}[b] ($m^2\ g^{-1}$)	V_P[b] (mL g^{-1})	C[c] (at.%)	O[c] (at.%)	C/O atom ratio[c]	Residual carbon[d] (%)
Graphite	1348.9	1574.5	0.16	–	–	–	–	–	–	–
GO	1336.7	1588.7	0.97	46.4	–	–	72.18	27.82	2.59	44.3
G250	1331.1	1591.5	1.42	308.8	8.34	3.578	89.70	10.30	8.71	62.2
G600	1330.7	1587.9	1.47	293.1	NA	2.905	91.19	8.81	10.35	71
G800	–	–	–	302.2	NA	3.192	95.34	4.66	20.46	79.7
G1000	1331.1	1594.8	1.44	434.1	NA	3.138	97.06	2.94	33.05	84.8

Reprinted from Ref. [55], Copyright 2012, with permission from Elsevier

[a]Obtained from Raman spectroscopy

[b]Calculated from N_2 physisorption isotherm

[c]Quantified by XPS

[d]Obtained from TGA (from room temperature to 1000 °C with rate of 10 °C/min in Ar)

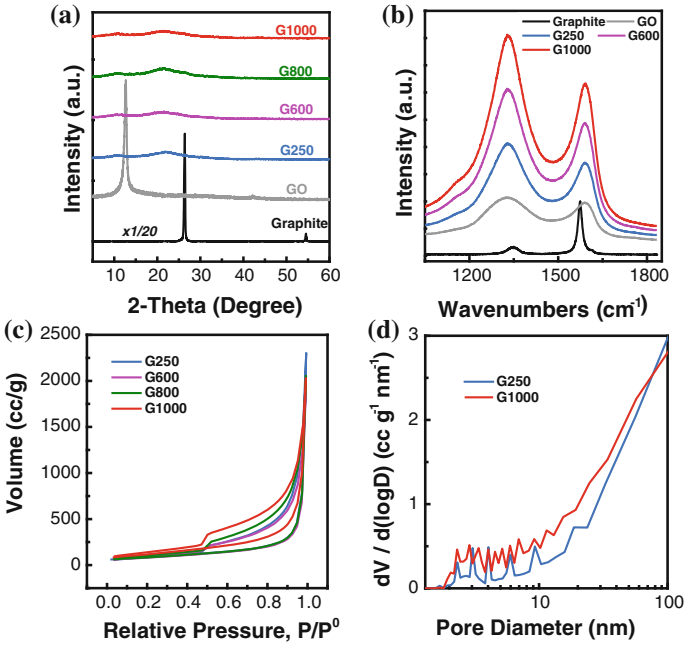

Fig. 2.2 **a** XRD pattern and **b** Raman spectrum evolution from GO to TRG; **c** N_2 physical adsorption isotherm and **d** BJH adsorption pore size distribution of G250 and G1000. Reprinted from Ref. [55], Copyright 2012, with permission from Elsevier

shift to higher frequencies of peak position and the intensity ratio of D and G bands increases, which can be attributed to some in-plane sp^2 carbons in graphitic domain transform into distorted sp^3 carbons in amorphous domain. Thus, a pristine graphitic region may be divided into several isolated sp^2 domains and double bonds by these amorphous domains, which resonate at higher frequencies than the G band of graphite. Besides, the newly introduced amorphous domains will also cause the increase in the intensity ratio of D and G band [36–39]. Second, a gradual sharpening of G band as well as increasing of I_D/I_G ratio (1.4–1.5) are observed from GO to G1000. During annealing, the desorption of oxygen bonded saturated sp^3 carbons as CO_2 and CO would leave various topological defects and vacancies in the graphene lattice, while a simultaneous 'self-healing' of graphitic lattice ('re-graphitization') will occur owing to the continuous deoxygenation.

FTIR spectrum is employed to characterize the surface functionalities of graphene qualitatively. As shown in Fig. 2.3, GO shows a wide hydroxyl stretching vibration mode in carboxyl, phenol, and/or intercalated H_2O (ν O–H) at 3400 cm^{-1}, and the C=O stretching vibration from carbonyl and carboxyl groups (ν C=O) at 1710 cm^{-1}. The characteristic peak at 1620 cm^{-1} corresponds to the components from the skeletal vibrations of un-oxidized graphitic domains

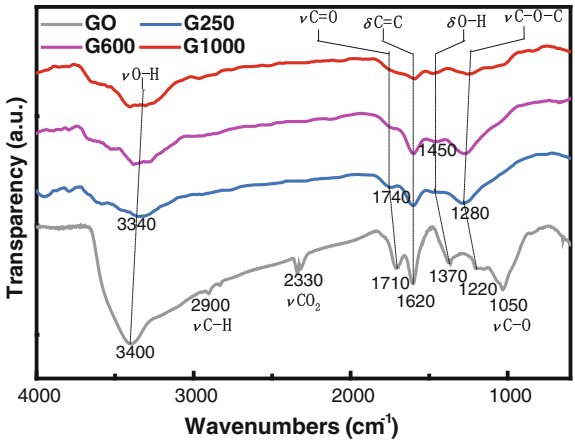

Fig. 2.3 The FTIR spectra of GO and TRG (G250, G600, and G1000). Reprinted from Ref. [55], Copyright 2012, with permission from Elsevier

(δ C=C). While the bands at 1370, 1220, and 1050 cm^{-1} can be linked to the carboxyl C–O deformation vibrations (δ O–H), epoxy, and/or ether type C–O–C (ν C–O–C), and alkoxy C–O stretching vibrations (δ C–O), respectively [40–42]. Besides, the thermal reduction temperature has a remarkable impact on the oxygen-containing groups. As the thermal reduction process deepened at higher temperature, the oxygen-containing groups are diminishing significantly. For G250 and G600, the ν O–H peak is blue shifted to 3340 cm^{-1} with a weaker intensity, while the ν C–O–C is red shifted to 1280 cm^{-1} with a relative higher intensity. Such phenomenon is ascribed to the dehydration of some neighboring –OH species, which not only weaken the intramolecular hydrogen bonding but also introduce more thermally stable C–O–C species. Moreover, the ν C=O peak was remarkably diminished due to the decomposing of thermally unstable –COOH species. The remained peak, up shifted to 1740 cm^{-1}, can be a trace of C=O groups in quinones, ketones, and lactones [43]. The vanishing of ν C–O peak implies the removal or transformation of oxygen saturated sp^3 carbon sites whereas the remained strong C=C mode is due to the effective repairing of conjugated C=C in sp^2 graphitic regions. Finally, G1000 shows a characteristic of infrared inert, which can be attributed to the increase of structural symmetry by intensive deoxygenation and thermal healing of graphitic domains at higher temperature.

The atomic percentage of C, O heteroatoms, as well as the C/O atomic ratio are calculated and summarized in Table 2.1. After thermal expansion of GO in high vacuum at 250 °C, the oxygen content significantly decreases to 10.30 at.% of G250 from 27.82 at.% of GO. As the annealing temperature increases, oxygen on the surface of TRGs are progressively removed with a final value of only 2.94 at.% for G1000 (Table 2.1), indicating a high degree of carbonization. The chemical state of

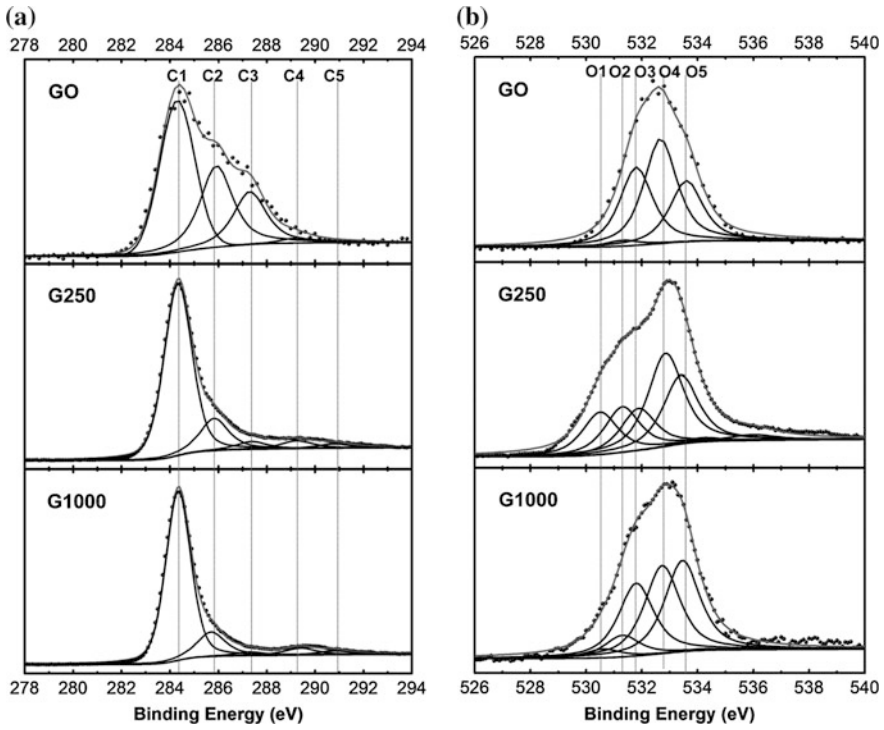

Fig. 2.4 **a** The C1s and **b** O1s XPS fine scan spectrum of GO, G250, and G1000. Reprinted from Ref. [55], Copyright 2012, with permission from Elsevier

the carbon and oxygen species on the surface of GO and TRGs was further studied by XPS analysis. As shown in Fig. 2.4a, b, various C (C1–C5) and O (O1–O5) components in GO, G250 and G1000 are determined by fitting the C1s and O1s fine scan spectra. C1 (284.4 eV), C2 (285.9 eV), C3 (287.4 eV), C4 (289.3 eV), and C5 (290.8 eV) components are belong to C–C, C–O, C=O, C(O)O related groups and graphitic shake-up satellites, respectively. O1 (530.4 eV), O2 (531.2 eV), O3 (531.9 eV), O4 (532.8 eV), and O5 (533.4 eV) components are assigned to quinone-type, C(O)O, –C=O, –C–O, and –OH groups, respectively [39, 44, 45].

As shown in Table 2.2, the amounts of C–C components are significantly increased from 33.75 at.% of GO to 73.13 at.% of G1000, with a simultaneous improvement of the graphitization degree, while the abundance of C–O and C=O related species are correspondingly decreased. Correlated with the Raman spectra and FTIR curves, the fitting results of C1s spectrum indicate that the oxygen heteroatoms are gradually removed from the basal plane of graphene during the thermal exfoliation and further annealing process. This will be favorable for the restoration of sp^2 conjugated carbon lattice so as to enhance the electronic conductivity of final products. Further, the O1s peak fitting results are more reliable in

Table 2.2 Fitted results (at.%) of C1s XPS spectra of TRG

B.E. (eV)	C1 (284.4)	C2 (285.9)	C3 (287.4)	C4 (289.3)	C5 (290.8)
Assignment	C–C	C–O	C=O	C(O)O	Graphitic shake-up
GO	33.75	22.57	14.70	1.16	0.00
G250	64.98	14.82	3.81	4.04	2.26
G1000	73.13	14.19	2.07	4.49	2.60

Reprinted from Ref. [55], Copyright 2012, with permission from Elsevier

quantitating the relative accurate composition of different oxygen components in GO and TRGs. As shown in Table 2.3, the C=O components (mainly contributed by carboxyls and carbonyls) are remarkably reduced from 8.71 at.% of GO to 1.40 at.% of G250, while the C(O)O related components (mainly ascribed to anhydrides and lactones) are simultaneously increased from 0.66 of GO to 1.52 at.% of G250. Therefore, it is deduced that, a vast majority of unstable carboxylic groups in GO is either removed by thermal decarboxylation, or rather transformed into more thermally stable anhydrides and lactones during the vacuum promoted thermal expansion at 250 °C. It is worth mentioning that, about 1.41 at.% of quinone-type oxygens are also introduced to graphene after the thermal-induced exfoliation. Since some unadulterated free radicals will generate on the edge and basal plane of graphene during the elimination of functionalities, the oxygen atoms in the circumstance are tend to adsorb on these radicals to form the carbene-type coordinate intermediates. In order to give thermodynamically stable quinones, the rearrangement reactions take place between the delocalized π electrons from the basal plane of graphene and these coordinate intermediates [46, 47]. Meanwhile, a majority of C–O and O–H components are also eliminated by the intramolecular dehydration between hydroxylic and/or carboxylic groups. After carbonized at 1000 °C, most of the thermally unstable oxygen components in graphene have been thoroughly removed. As a result, the O–H, C–O, and C=O related functional groups, which are, respectively, transformed into thermally more stable isolated phenols, ethers, and carbonyls, finally become the major components in G1000.

The thermogravimetric analysis-mass spectrometry (TG-MS) is conducted in Ar atmosphere to examine the thermochemistry of GO and TRGs (Fig. 2.5). As shown in Table 2.1, after annealing at various temperatures from 250 to 1000 °C, the residual carbon ratios are increased progressively from 44.3 % of G250 to 84.8 % of G1000, which indicates the stabilization effect on graphene by thermal annealing. The sweep gases from TG are further analyzed by mass spectrometry and various fragments with m/z = 12.3 (radical C), 16.26 (radical O), 18.16 (H_2O), 28.18 (CO), and 44.09 (CO_2) are assigned (Fig. 2.5b–f). From GO to G1000, all the evolved gases fragments are dramatically decreased with the blue

Table 2.3 Fitted results (at.%) of O1s XPS spectra of TRG

B.E. (eV)	O1 (530.5)	O2 (531.2)	O3 (531.9)	O4 (532.7)	O5 (533.5)
Assignment	Quinone	C(O)O	C=O	C–O	O–H
GO	0.00	0.66	8.71	11.66	6.79
G250	1.41	1.52	1.40	3.09	2.28
G1000	0.11	0.27	0.90	1.09	1.13

Reprinted from Ref. [55], Copyright 2012, with permission from Elsevier

shifts of decomposing temperature, which implies the improved stability of graphene at higher carbonization process.

The accompanying structural evolution and the surface chemistry of carbons have been widely investigated in the past several decades [47–49]. However, Graphene, as a single layer of sp^2 carbon atoms and two-dimensional carbon macromolecule, is giving new insights toward the surface chemistry of carbon materials [18, 46, 50, 51]. Since different oxygen-containing functional groups display distinct decomposing behavior during carbonization process, the surface properties of carbon are mainly dependent on the maximum temperature employed in the annealing process, as [52, 53]. It is reported that the sequence of thermal stability for various oxygen-containing groups on carbon surface and corresponding gases evolved during the decomposing are: carbonyl/quinones (CO) > lactones (CO_2) > phenols (CO) > anhydrides (CO and CO_2) > carboxylic acids (CO_2) [18, 52]. Herein, several evolution pathways for surface oxygen functionalities are proposed according to the FTIR, XPS, and TG-MS results in Fig. 2.6. The deoxygenation and reduction during annealing process is roughly divided into five stages: (I) from 30 to 150 °C, the physically adsorbed and intercalated water is removed ('physical' water); (II) from 150 to 400 °C, the intermolecular dehydration occur between neighboring carboxylic and/or hydroxyl groups, to transform into thermally stable lactones, anhydrides, ethers, and carbonyls as well as release abundant H_2O ('chemical' water). At the same time, the decarboxylation of individual carboxylic groups release abundant CO_2 [49]; (III) from 400 to 600 °C, the anhydrides decompose to release both CO_2 and CO, while the individual phenols decompose to evolve CO; (IV) from 600 to 800 °C, the lactones and individual ether desorb as CO_2 and CO, respectively, and (V) from 800 to 1000 °C, the most stable carbonyls and quinones will decompose to release CO [52].

2.3.2 Electrochemical Performance

The electrochemical performances of TRG-based supercapacitor electrodes were characterized by a three-electrode system in 6.0 M KOH aqueous electrolyte. Figure 2.7a shows typical CV curves of all TRGs at a scan rate of 3.0 mV s^{-1}. It can be observed that all of them exhibit the prominent capacitive behaviors, as the

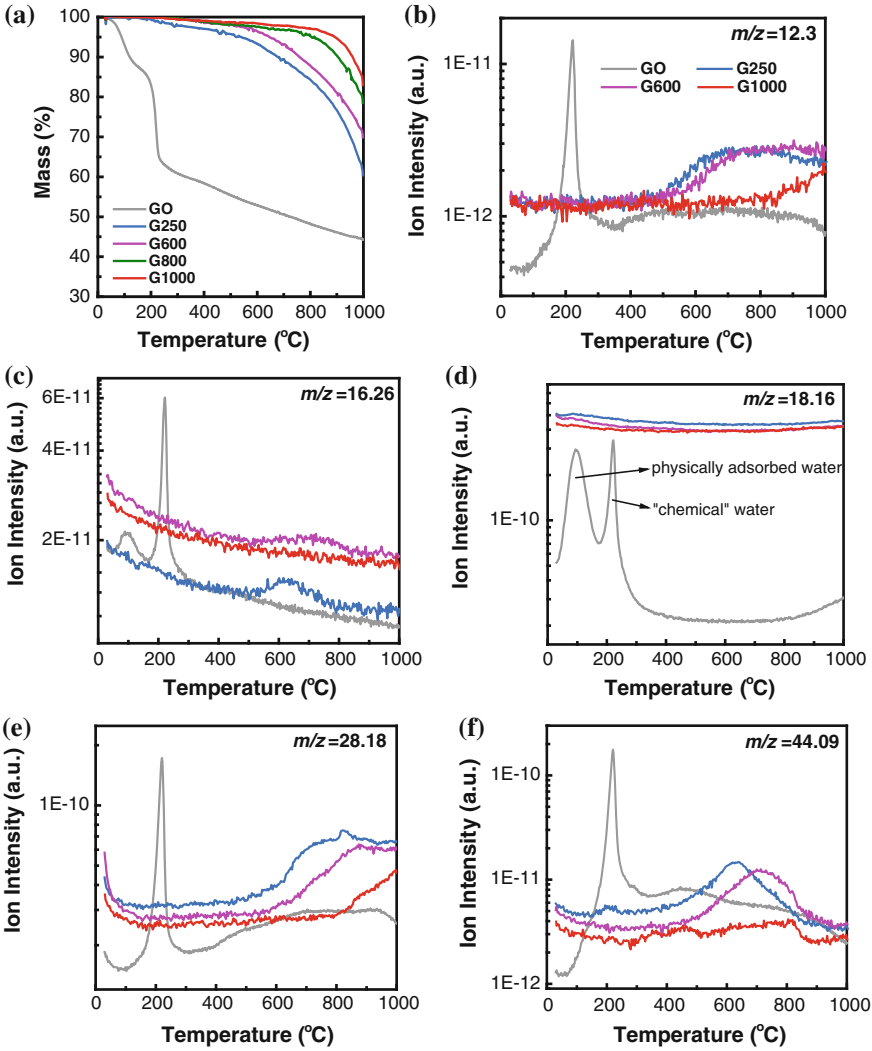

Fig. 2.5 **a–f** The TG-MS analysis of GO and TRGs. Reprinted from Ref. [55], Copyright 2012, with permission from Elsevier

sign of current reverse immediately upon reversal of the potential sweep. The capacitive current (i_M, A g^{-1}) drops quickly from G250 to G1000, while the CVs approach nearly ideal rectangular shape for, indicating an pronounced contribution of EDLC for the G1000-based electrode. The specific capacitance C_F (F g^{-1}) and C_s (F m^{-2}) as calculated from CVs (Fig. 2.7a) and S_{BET} (Table 2.1) are summarized in Fig. 2.7b. It can be seen that the initial CF and CS of G250 reach 170.5 F g^{-1} and 0.56 F m^{-2} at a low scan rate of 3 mV s^{-1}, respectively. However,

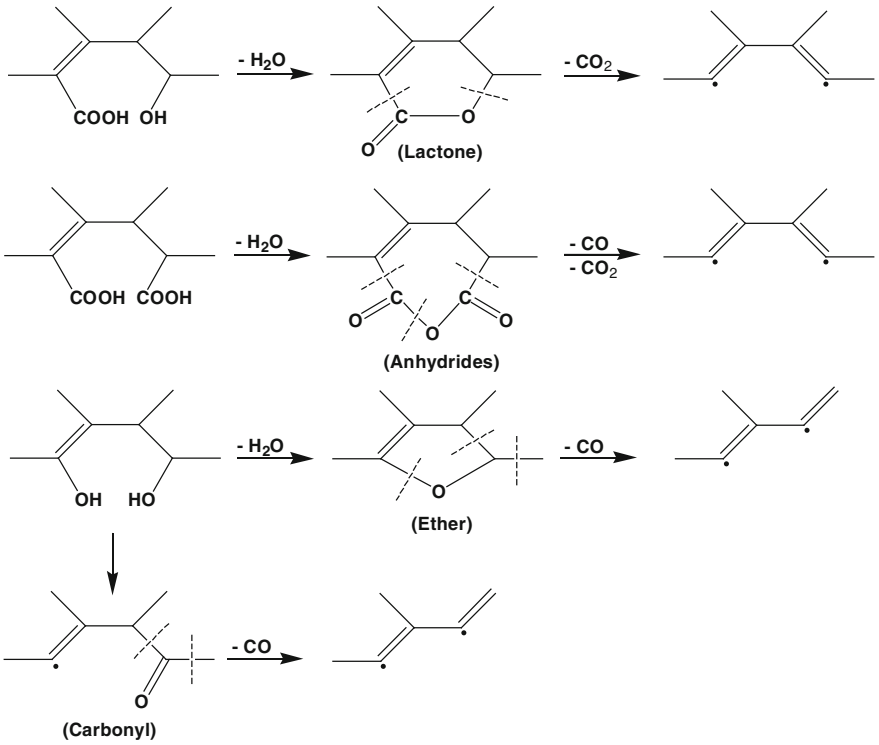

Fig. 2.6 Proposed pathway for transformation and evolution of oxygen-containing functional groups during thermal expansion of GO into TRGs. Reprinted from Ref. [55], Copyright 2012, with permission from Elsevier

the values decrease quickly for the further annealed TRGs. The G1000 presents a very poor specific capacitance ($C_F = 47.5$ F g^{-1}, $C_S = 0.11$ F m^{-2}). On one hand, most of the PC is eliminated owing to the intensive removal of PC-active oxygen-containing functional groups at higher temperature; on the other hand, the electronic conductivity of the electrode is significantly enhanced with the progressive re-graphitization of the carbon lattice in graphene basal plane.

In order to evaluate the fast charge/discharge abilities of the materials, the rate-dependent CVs for G250 and G1000 over a range of scan rates from 3 to 500 mV s^{-1} are examined as shown in Fig. 2.7c and d, respectively. When the scan rate increases, the CVs of G250 distort quickly to a willow-leaf-like shape with a voltage delay (ΔU) of ~0.2 V at 500 mV s^{-1}. This is attributed to the relatively slow charge/discharge kinetics from Faradaic reaction of surface functionalities compared with EDLC. At the same time, the CVs of G1000 still retain a rectangular-like shape and undergo much less distortion (ΔU ~0.06 V) at 500 mV s^{-1}, due to a quick response of EDLC with a pure electrostatic character. The specific capacitance values calculated from CVs at different scan rates are

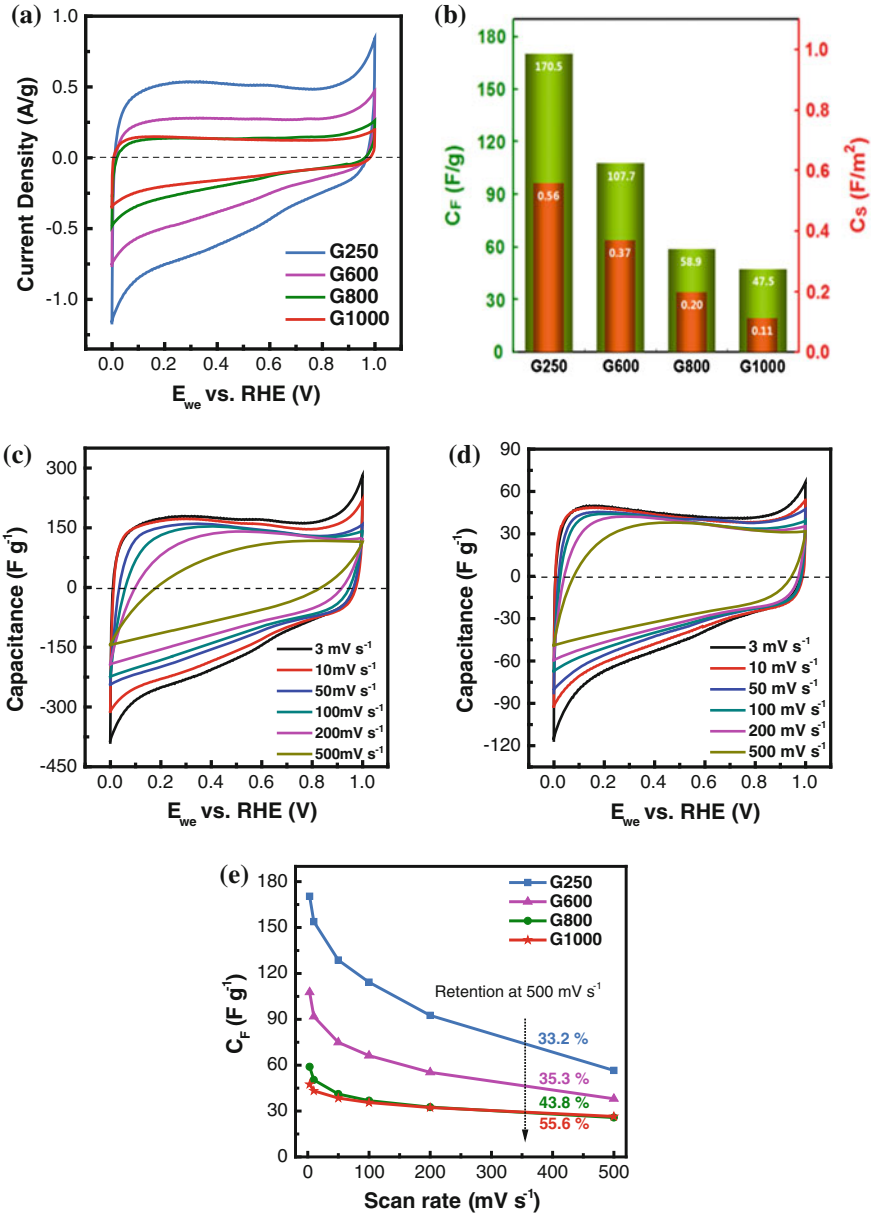

Fig. 2.7 **a** Evolution of CVs at 3.0 mV s^{-1} from G250 to G1000; CVs of **b** G250 and **c** G1000 with sweep rates from 3.0 to 500 mV s^{-1}; **d** Specific capacitance C_F (F g^{-1}) and C_s (F m^{-2}) for G250 to G1000 at 3.0 mV s^{-1}; **e** C_F versus sweep rates for G250 to G1000. Reprinted from Ref. [55], Copyright 2012, with permission from Elsevier

Table 2.4 Fitting results of internal components for graphene based electrodes

Sample	R_i (Ω)	R_c (Ω)	C_c (F/g)	W (Ω $s^{-1/2}$)	C_d (F/g)
G250	1.93	0.43	0.39	1.07	135.14
G1000	0.89	0.34	0.23	1.12	34.47

Reprinted from Ref. [55], Copyright 2012, with permission from Elsevier

shown in Fig. 2.7e. Compared with the other TRGs, G250 exhibits the highest capacitive value within the whole range of scan rates. Although the initial C_F at 3 mV s^{-1} is remarkably reduced for the higher temperature annealed TRGs, the retention of C_F at a high scan rate of 500 mV s^{-1} is gradually increased from 33.2 % of G250 to 55.6 % of G1000. With the increase of scan rates, the EDLC becomes the primary electrochemical behavior of the electrodes owing to the delay of potential during reversing scan, which is related to a kinetically slow process involved during charging/discharging the PC [1].

Figure 2.8a clearly shows the GC curves of TRGs at the current density of 1.0 A g^{-1}. The C_F calculated from the discharge curves of G250, G600, G800, and G1000 are 167.3, 98.3, 49.4, and 42.6 F g^{-1}, while the voltage drop (IR_{drop}) at the initiation of the discharge is 9.6, 9.9, 8.1, and 8.7 mV, respectively, indicating a very low equivalent series resistance (ESR) in the test cell. Figure 2.8b exhibits Nyquist plots of G250 and G1000. Meanwhile, an equivalent circuit model in inset of Fig. 2.8b is introduced to simulate the capacitive and resistive elements of the cells under analysis, which contain the internal resistance of the TRG-based electrode (R_i), the capacitance and resistance due to contact interface (C_c and R_c), a Warburg diffusion element attributable to the ion migration through the graphene (Z_w), and the capacitance inside the pores (C_d) [54]. The corresponding results are presented in Table 2.4. In accordance with the microstructural and chemical evolution of graphene, the internal resistance (R_i) of G1000 (0.89 Ω) is remarkably lower than that of G250 (1.93 Ω), which is ascribed to the sp^2 conjugated carbon lattice significantly restored during the annealing process to increase charge carrier density. Moreover, comparing with G250 (Z_w = 1.07 Ω $s^{-1/2}$), G1000 exhibits a slightly higher Warburg diffusion resistance (Z_w = 1.12 Ω $s^{-1/2}$), which is attributed to the hamper of ion transfer between the inner channel of honeycomb and the aqueous electrolyte, as the wettability of the graphene surface is remarkably tampered after removal of most hydrophilic oxygen groups. Finally, the G250 electrode delivers the inner-porous capacitance of 135.1 F g^{-1}, whereas only about a quarter of the value of G250 (34.5 F g^{-1}) is obtained for the G1000 electrode, which imply oxygen functional groups play a crucial role in both introducing abundant peseudocapacitance as well as improving the surface efficiency of graphene during electrochemical cycling.

The contribution of pseudocapacitance from oxygen functionalities is based on a reversible Faradic redox mechanism [1, 3]. The basal plane of a TRG sheet is composed of distorted sp^3 carbons decorated by various oxygen functionalities and numerous sp^2 graphitic domains [50]. The inductive effects originated from the

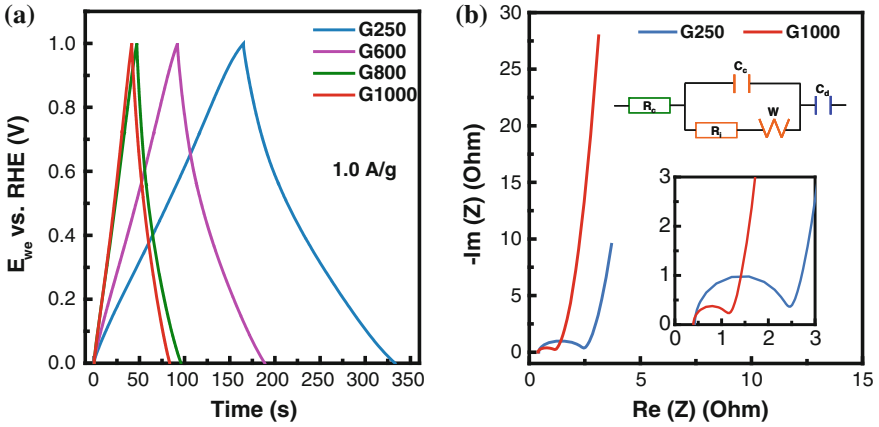

Fig. 2.8 **a** Galvanostatic charge/discharge curves and **b** Nyquist plot of G250 and G1000; *Inserted figure* show the enlarged Nyquist plot and equivalent circuit model. Reprinted from Ref. [55], Copyright 2012, with permission from Elsevier

oxygen atoms will lead to the polarization of some C–C bonds, while the delocalized electrons within the sp^2 domains supply a low resistant channel for charge transfer within the electrode. Thus, the reversible redox reactions are likely to occur on these polarized sites during charging/discharging process (Fig. 2.9).

Comparing with basic functional groups (Fig. 2.9a, d), it is believed that the acidic sites (Fig. 2.9b, c) on carbon play a more dominant role in the alkaline KOH electrolyte. The abundant carboxylic and phenolic groups, which are usually thermally unstable, can be well maintained at a mild annealing temperature. However, with the temperature increasing, these oxygen-containing functional groups will be removed or transformed into basic sites, which are adverse to the pseudocapacitive reactions. This is the reason that the mild annealed G250, which not only possesses the highest oxygen content, but also own abundant acidic sites, shows extremely high electrochemical performance as supercapacitor electrode materials.

In order to completely determine the electrochemical performance of TRGs, a Ragone plot is exhibited in Fig. 2.10a. The energy and power densities are calculated from GC curves of a supercapacitor with a cell-voltage window of 1.0 V. It is worth noting that G250 exhibits the best electrochemical performance in energy storage among the TRGs-based electrodes, with a maximum energy density of 11.6 Wh kg^{-1} corresponding to power density of 250 W kg^{-1}. These results are in good agreement with the capacitance performance as calculated by CV curves. When the power density reaches as high as 5000 W kg^{-1}, it still owns an energy density of no less than 7.8 Wh kg^{-1}.

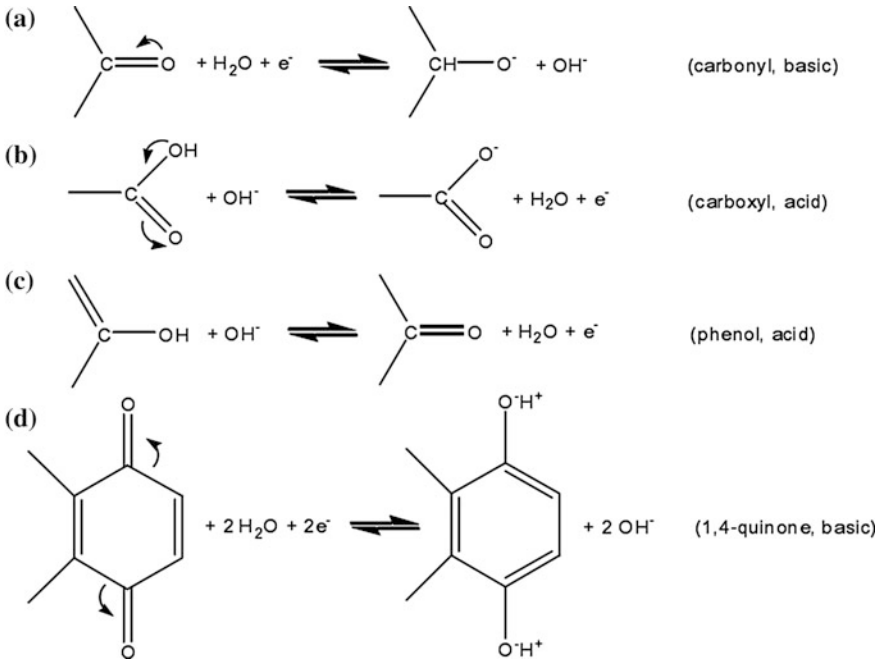

Fig. 2.9 Proposed reversible pseudo-capacitive reactions of various oxygen-containing functional sites with its acid-base property in the aqueous electrolyte. Reprinted from Ref. [55], Copyright 2012, with permission from Elsevier

In order to evaluate the cycling stability of G250 and G1000 electrodes, repeating CV charge/discharge process were performed at a scan rate of 50 mV s^{-1} between 0 V and 1 V in 6 M KOH aqueous electrolyte. As shown in Fig. 2.10b, after 3000 cycles, the specific capacitance of G250 was reduced to 94.7 % of the initial cycle, while G1000 still retains a high capacitive retention of as high as 99.5 %. The disparity of cycling stability between G250 and G1000 is ascribed to the difference in surface chemistry for TRGs at different carbonation stages. Comparing with G1000, G250 owns a much higher density of oxygen functional groups, especially for the unstable acidic carboxyls, which may be neutralized and diminished by alkaline KOH during repeating charging/discharging cycles, resulting in the loss of PC. Overall, comparing with the other energy storage devices which often suffer from a short cycle life due to irreversible physical and/or chemical changes; TRGs-based supercapacitor is still very attractive for its prominent durability and stability.

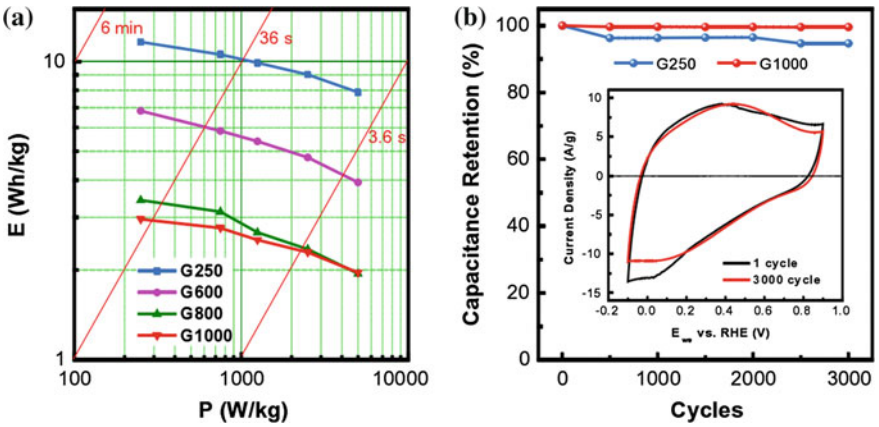

Fig. 2.10 Energy storage performance of TRGs: **a** Ragone plot as calculated from GC results under current density of 1, 3, 5, 10 and 20 A g^{-1}; **b** Cycling performance of G250 and G1000. *Inset* shows the 1 and 3000 cycle CV of G250 at a scan rate of 50 mV s^{-1} in 6.0 M KOH. Reprinted from Ref. [55], Copyright 2012, with permission from Elsevier

2.4 Conclusions

In this study, thermally reduced graphene (TRG) with adjustable surface chemistry was prepared by vacuum promoted thermal expansion of GO and subsequent annealing at different temperatures. After thermal expansion of GO in high vacuum at 250 °C, the C=O components (mainly ascribed to carboxyls and carbonyls) are dramatically decreased from 8.71 at.% of GO to only 1.40 at.% of G250, whereas the C(O)O related components (mainly contributed by anhydrides and lactones) are simultaneously increased from 0.66 at.% of GO to 1.52 at.% of G250. After carbonization at 1000 °C, most oxygen components in TRG have been removed. The O–H, C–O, and C=O related functional groups, which belong respectively to thermally more stable isolated phenols, ethers, and carbonyls, finally become the major components in G1000. Besides, the desorption of oxygen bonded carbons as CO_2 and CO produces large amount of topological defects and vacancies in the graphene lattice, with a simultaneous 'self-healing' of graphitic lattice ('re-graphitization'). The TRGs were further applied as electrodes of supercapacitor. The studies showed that the structural evolution induced by thermal annealing plays a key role in determining the electrochemical performance of TRGs towards supercapacitor applications. The oxygen functional groups can significantly enhance the capacitance performance of TRGs by introducing abundant PC-active sites through reversible Faradic redox reactions. It is worth noting that no obvious capacitance loss is observed over 3000 charge/discharge cycles, clearly demonstrating good cycling durability. TRGs-based supercapacitor will benefit the application of graphene in advanced energy storage.

References

1. Dell RM, Rand DAJ. Energy storage-a key technology for global energy sustainability. J Power Sources. 2001;100:2–17.
2. Conway BE. Electrochemical supercapacitors: scientific fundamentals and technological apllication. Dordrecht: Kluwer Academic/Plenum; 1999.
3. Frackowiak E. Carbon materials for supercapacitor application. Phys Chem Chem Phys. 2007;9(15):1774–85.
4. Pandolfo AG, Hollenkamp AF. Carbon properties and their role in supercapacitors. J Power Sources. 2006;157(1):11–27.
5. Su DS, Schlogl R. Nanostructured carbon and carbon nanocomposites for electrochemical energy storage applications. ChemSusChem. 2010;3(2):136–68.
6. Kotz R, Carlen M. Principles and applications of electrochemical capacitors. Electrochim Acta. 2000;45(15–16):2483–98.
7. An SJ, Zhu YW, Lee SH, Stoller MD, Emilsson T, Park S, et al. Thin film fabrication and simultaneous anodic reduction of deposited graphene oxide platelets by electrophoretic deposition. J Phys Chem Lett. 2010;1(8):1259–63.
8. Zhu Y, Murali S, Stoller MD, Ganesh KJ, Cai W, Ferreira PJ, et al. Carbon-based supercapacitors produced by activation of graphene. Science. 2011;332(6037):1537–41.
9. Su FY, You CH, He YB, Lv W, Cui W, Jin FM, et al. Flexible and planar graphene conductive additives for lithium-ion batteries. J Mater Chem. 2010;20(43):9644–50.
10. Wu Z-S, Ren W, Wen L, Gao L, Zhao J, Chen Z, et al. Graphene anchored with Co_3O_4 nanoparticles as anode of lithium ion batteries with enhanced reversible capacity and cyclic performance. ACS Nano. 2010;4(6):3187–94.
11. Wu Z-S, Wang D-W, Ren W, Zhao J, Zhou G, Li F, et al. Anchoring hydrous RuO_2 on graphene sheets for high-performance electrochemical capacitors. Adv Funct Mater. 2010;20(20):3595–602.
12. McAllister MJ, Li J-L, Adamson DH, Schniepp HC, Abdala AA, Liu J, et al. Single sheet functionalized graphene by oxidation and thermal expansion of graphite. Chem Mater. 2007;19(18):4396–404.
13. Zhu Y, Stoller MD, Cai W, Velamakanni A, Piner RD, Chen D, et al. Exfoliation of graphite oxide in propylene carbonate and thermal reduction of the resulting graphene oxide platelets. ACS Nano. 2010;4(2):1227–33.
14. Lv W, Tang D-M, He Y-B, You C-H, Shi Z-Q, Chen X-C, et al. Low-temperature exfoliated graphenes: vacuum-promoted exfoliation and electrochemical energy storage. ACS Nano. 2009;3(11):3730–6.
15. Zhang HB, Wang JW, Yan Q, Zheng WG, Chen C, Yu ZZ. Vacuum-assisted synthesis of graphene from thermal exfoliation and reduction of graphite oxide. J Mater Chem. 2011;21(14):5392–7.
16. Wu Z-S, Ren W, Gao L, Zhao J, Chen Z, Liu B, et al. Synthesis of graphene sheets with high electrical conductivity and good thermal stability by hydrogen arc discharge exfoliation. ACS Nano. 2009;3(2):411–7.
17. Wu Z-S, Ren W, Gao L, Liu B, Jiang C, Cheng H-M. Synthesis of high-quality graphene with a pre-determined number of layers. Carbon. 2009;47(2):493–9.
18. Bagri A, Mattevi C, Acik M, Chabal YJ, Chhowalla M, Shenoy VB. Structural evolution during the reduction of chemically derived graphene oxide. Nat Chem. 2010;2(7):581–7.
19. Pumera M. Graphene-based nanomaterials and their electrochemistry. Chem Soc Rev. 2010;39(11):4146–57.
20. Yan J, Wei T, Shao B, Fan ZJ, Qian WZ, Zhang ML, et al. Preparation of a graphene nanosheet/polyaniline composite with high specific capacitance. Carbon. 2010;48(2):487–93.
21. Wang HL, Hao QL, Yang XJ, Lu LD, Wang X. A nanostructured graphene/polyaniline hybrid material for supercapacitors. Nanoscale. 2010;2(10):2164–70.

22. Zhang LL, Zhou R, Zhao XS. Graphene-based materials as supercapacitor electrodes. J Mater Chem. 2010;20(29):5983–92.
23. Sun YQ, Wu QO, Shi GQ. Graphene based new energy materials. Ener Environ Sci. 2011;4(4): 1113–32.
24. Fan ZJ, Yan J, Zhi LJ, Zhang Q, Wei T, Feng J, et al. A three-dimensional carbon nanotube/ graphene sandwich and its application as electrode in supercapacitors. Adv Mater. 2010;22(33): 3723–8.
25. Huang X, Yin ZY, Wu SX, Qi XY, He QY, Zhang QC, et al. Graphene-based materials: synthesis, characterization, properties, and applications. Small. 2011;7(14):1876–902.
26. Guo SJ, Dong SJ. Graphene nanosheet: synthesis, molecular engineering, thin film, hybrids, and energy and analytical applications. Chem Soc Rev. 2011;40(5):2644–72.
27. Inagaki M, Konno H, Tanaike O. Carbon materials for electrochemical capacitors. J Power Sources. 2010;195(24):7880–903.
28. Zhu YW, Murali S, Cai WW, Li XS, Suk JW, Potts JR, et al. Graphene and graphene oxide: synthesis, properties, and applications. Adv Mater. 2010;22(35):3906–24.
29. Fan ZJ, Yan J, Wei T, Zhi LJ, Ning GQ, Li TY, et al. Asymmetric supercapacitors based on graphene/MnO_2 and activated carbon nanofiber electrodes with high power and energy density. Adv Funct Mater. 2011;21(12):2366–75.
30. Chen CM, Yang Q-H, Yang Y, Lv W, Wen Y, Hou P-X, et al. Self-assembled free-standing graphite oxide membrane. Adv Mater. 2009;21(29):3007–11.
31. Vix-Guterl C, Frackowiak E, Jurewicz K, Friebe M, Parmentier J, Béguin F. Electrochemical energy storage in ordered porous carbon materials. Carbon. 2005;43(6):1293–302.
32. Vinu A, Ariga K, Mori T, Nakanishi T, Hishita S, Golberg D, et al. Preparation and characterization of well-ordered hexagonal mesoporous carbon nitride. Adv Mater. 2005;17(13):1648–52.
33. Zhao XC, Wang AQ, Yan JW, Sun GQ, Sun LX, Zhang T. Synthesis and electrochemical performance of heteroatom-incorporated ordered mesoporous carbons. Chem Mater. 2010;22(19):5463–73.
34. Huang CH, Doong RA, Gu D, Zhao DY. Dual-template synthesis of magnetically-separable hierarchically-ordered porous carbons by catalytic graphitization. Carbon. 2011;49(9):3055–64.
35. Schniepp HC, Li J-L, McAllister MJ, Sai H, Herrera-Alonso M, Adamson DH, et al. Functionalized single graphene sheets derived from splitting graphite oxide. J Phys Chem B. 2006;110(17):8535–9.
36. Stankovich S, Dikin DA, Piner RD, Kohlhaas KA, Kleinhammes A, Jia Y, et al. Synthesis of graphene-based nanosheets via chemical reduction of exfoliated graphite oxide. Carbon. 2007;45(7):1558–65.
37. Pei SF, Zhao JP, Du JH, Ren WC, Cheng HM. Direct reduction of graphene oxide films into highly conductive and flexible graphene films by hydrohalic acids. Carbon. 2010;48(15):4466–74.
38. Kudin KN, Ozbas B, Schniepp HC, Prud'homme RK, Aksay IA, Car R. Raman spectra of graphite oxide and functionalized graphene sheets. Nano Lett. 2007;8(1):36–41.
39. Chen CM, Huang JQ, Zhang Q, Gong WZ, Yang QH, Wang MZ, et al. Annealing a graphene oxide film to produce a free standing high conductive graphene film. Carbon. 2012;50(2):659–67.
40. Stankovich S, Piner RD, Nguyen ST, Ruoff RS. Synthesis and exfoliation of isocyanate-treated graphene oxide nanoplatelets. Carbon. 2006;44(15):3342–7.
41. Xiao J, Mei D, Li X, Xu W, Wang D, Graff GL, et al. Hierarchically porous graphene as a lithium–air battery electrode. Nano Lett. 2011;11(11):5071–8.
42. Lai LF, Chen LW, Zhan D, Sun L, Liu JP, Lim SH, et al. One-step synthesis of NH_2-graphene from in situ graphene-oxide reduction and its improved electrochemical properties. Carbon. 2011;49(10):3250–7.
43. Yue L, Li W, Sun F, Zhao L, Xing L. Highly hydroxylated carbon fibres as electrode materials of all-vanadium redox flow battery. Carbon. 2010;48(11):3079–90.

44. Arrigo R, Havecker M, Wrabetz S, Blume R, Lerch M, McGregor J, et al. Tuning the acid/base properties of nanocarbons by functionalization via amination. J Am Chem Soc. 2010;132(28): 9616–30.
45. Yan J, Wei T, Shao B, Ma FQ, Fan ZJ, Zhang ML, et al. Electrochemical properties of graphene nanosheet/carbon black composites as electrodes for supercapacitors. Carbon. 2010;48(6): 1731–7.
46. Radovic LR. Active sites in graphene and the mechanism of CO_2 formation in carbon oxidation. J Am Chem Soc. 2009;131(47):17166–75.
47. Menendez JA, Xia B, Phillips J, Radovic LR. On the modification and characterization of chemical surface properties of activated carbon: microcalorimetric, electrochemical, and thermal desorption probes. Langmuir. 1997;13(13):3414–21.
48. Serp P, Figueiredo JL. Surface chemistry of carbon materials. In: Carbon materials for catalysis (Chap. 2), p. 45.
49. Menéndez JA, Phillips J, Xia B, Radovic LR. On the modification and characterization of chemical surface properties of activated carbon: in the search of carbons with stable Basic properties. Langmuir. 1996;12(18):4404–10.
50. Dreyer DR, Park S, Bielawski CW, Ruoff RS. The chemistry of graphene oxide. Chem Soc Rev. 2010;39(1):228–40.
51. Loh KP, Bao Q, Ang PK, Yang J. The chemistry of graphene. J Mater Chem. 2010;20(12): 2277.
52. Figueiredo JL, Pereira MFR. The role of surface chemistry in catalysis with carbons. Catal Today. 2010;150(1–2):2–7.
53. Acik M, Lee G, Mattevi C, Pirkle A, Wallace RM, Chhowalla M, et al. The role of oxygen during thermal reduction of graphene oxide studied by infrared absorption spectroscopy. J Phys Chem C. 2011;115(40):19761–81.
54. Xu GH, Zheng C, Zhang Q, Huang JQ, Zhao MQ, Nie JQ, et al. Binder-free activated carbon/carbon nanotube paper electrodes for use in supercapacitors. Nano Res. 2011;4(9):870–81.
55. Chen CM, Zhang Q, Yang MG, Huang CH, Yang YG, Wang MZ. Structural evolution during annealing of thermally reduced graphene nanosheets for application in supercapacitors. Carbon. 2012;50(10):3572–84.

http://www.springer.com/978-3-662-48674-0

Surface Chemistry and Macroscopic Assembly of Graphene for Application in Energy Storage

Chen, C.-M.

2016, XIII, 146 p. 73 illus., 18 illus. in color., Hardcover
ISBN: 978-3-662-48674-0